Flow, Turbulence and Combustion
https://doi.org/10.1007/s10494-024-00600-z

RESEARCH

Detection of Energetic Low Dimensional Subspaces in Spatio-Temporal Space in Turbulent Pipe Flow

Amir Shahirpour[1] · **Christoph Egbers**[2] · **Jörn Sesterhenn**[1]

Received: 3 June 2024 / Accepted: 21 October 2024

Abstract
Low dimensional subspaces are extracted out of highly complex turbulent pipe flow at $Re_\tau = 181$ using a Characteristic Dynamic Mode Decomposition (CDMD). Having lower degrees of freedom, the subspaces provide a more clear basis to detect events which meet our understanding of large-scale coherent structures. To this end, a temporal sequence of state vectors from direct numerical simulations are rotated in space-time such that persistent dynamical modes on a hyper-surface are found travelling along its normal in space-time, which serves as the new time-like coordinate. The main flow features are captured with a minimal number of modes on a moving frame of reference whose velocity matches that of the most energetic scale. Reconstruction of the candidate modes in physical space gives the low rank model of the flow. The structures living in this subspace have long life-times, posses wide range of length-scales and travel at group velocities close to that of the moving frame of reference. The modes within this subspace are highly aligned, but are separated from the remaining modes by larger angles. We are able to capture the essential features of the flow like the spectral energy distribution and Reynolds stresses with a subspace consisting of about 10 modes. The remaining modes are collected in two further subspaces, which distinguish themselves by their axial length scale and degree of isotropy.

Keywords Data driven model reduction · Dynamic mode decomposition · Turbulent pipe flow · Coherent structures

✉ Jörn Sesterhenn
joern.sesterhenn@uni.bayreuth.de

Amir Shahirpour
amir.shahirpour@uni-bayreuth.de

Christoph Egbers
christoph.egbers@b-tu.de

[1] Lehrstuhl für Technische Mechanik und Strömungsmechanik, Universität Bayreuth, Universitätstr. 30, Bayreuth 95440, Bayern, Deutschland

[2] Lehrstuhl Aerodynamik und Strömungslehre, Brandenburgische Technische Universität Cottbus - Senftenberg, Siemens-Halske-Ring 15a, Cottbus 03046, Brandenburg, Deutschland

Published online: 18 December 2024

1 Introduction

Large-scale energetic coherent structures detected in turbulent flows have become an inseparable part of turbulence studies. Proof of their existence is promising as it implies that taking advantage of the notion of coherence can shed light on the high-dimensional turbulent flows with complex flow patterns. These structures contribute prominently to the turbulent kinetic energy while diffusing mass and momentum and carrying large desirable or undesirable effects such as better mixture or more drag (Marusic et al. 2010).

In spite of large number of studies in the last decade to understand their physical properties there is still limited consensus in the scientific community on how to define these structures, what they physically look like, how long they live and how their length scales depend on Reynolds numbers. It is not fully understood what they feed on, how their regeneration mechanism works and how they interact with each other or with near wall turbulence.

Three groups of structures are well distinguished in literature by their length scales and wall-normal locations. Near-wall streaks are known as manifestations of the wall cycle of turbulence and have mean span-wise spacing of $\lambda^+ = 100$ and mean stream-wise length of $\lambda_x^+ = 1000$ (Kline et al. 1967). Their origin and regeneration pattern has been the subject of many studies showing that they are formed by lift-up mechanism of the mean profile, mean shear and viscous diffusion (Chernyshenko and Baig 2005). Their self sustainability has been shown in studies like Jiménez and Moin (1991) where a minimal flow unit is simulated as the smallest channel flow that can maintain turbulence.

Large scale motions (LSMs) are described as motions whose coherence is maintained as a result of eddies travelling at the same group velocity (Kim and Adrian 1999). Measurements of Bailey and Smits (2010) show evidence for existence of such eddies in the outer layer being detached from the wall with small correlation with the near wall flow, whereas in the logarithmic region they are more likely to be attached to the wall. This suggests existence of attached LSMs in the near-wall region and detached ones in the outer layer. They are known to have stream-wise scale of 2-3 pipe radii and span-wise length scale of 1−1.5 radii (Guala et al. 2006).

Very Large-Scale Motions in pipe and channel flow (referred to as VLSMs by Adrian and coworkers) or superstructures in boundary layer flows (named by Marusic and coworkers), appear to be longer and have streamwise length scale of 8-20 pipe radii (Vallikivi et al. 2015). While they are mostly seen in the logarithmic layer in boundary layer flow, they appear in the outer layer of internal flows (Monty et al. 2009). Kim and Adrian (1999) interpret VLSM as a result of stream-wise alignment of LSMs which exist in the outer layer, whereas Álamo and Jiménez (2006) argue that their formation is the result of linear and nonlinear processes.

Interactions of LSMs with the near-wall structures has been the subject of several studies. Toh and Itano (2005) consider large-scale structures as part of the turbulence and argue that they feed on their interactions with the near-wall small-scale structures. Del Álamo and Jiménez (2006) on the other hand interpret them as self-sustained structures. Apart from their regeneration mechanism, many key questions concerning LSM and VLSM are still unanswered including a uniform scaling law for their identification as well as a clear understanding of their origin and evolution. Differing views on the origin and nature of low wave number VLSMs question their dependence on geometry and outer layer variables.

Spectral analysis has been one of the key approaches commonly used to learn about the properties of such structures. Their footprints can be followed by observing the

premultiplied velocity spectra which represent the energy distribution in the wave number space. At sufficiently large Reynolds numbers two outer peaks appear in contour plots of spectra which are associated with VLSM and LSM (Rosenberg et al. 2013). The signature of large-scale energetic structures are hereby followed and their length scales and energy content at different wall normal positions are determined.

The outer spectral peaks have been mostly observed via experimental measurements as the well-resolved numerical studies have been limited to lower Reynolds numbers due to high computational costs. Nevertheless, Pirozzoli et al. (2021) have extended this limit considerably to $Re_\tau = 6000$ and have shown that the present computations have reached a state where asymptotically high Reynolds number behaviour is starting to be seen. An example would be the DNS by Yao et al. (2023) where they clearly show the emergence of an energetic outer spectral peak at $Re_\tau = 5200$.

Taking advantage of the spectral footprint, Bauer et al. (2019) apply a two dimensional Fourier cut-off filter to separate the structures based on the their known length-scales to investigate which length scales are responsible for feeding the largest scales and which ones feed from them. Besides differing views on the nature and origin of turbulent structures, the suitable approach for their analysis is also still under debate. Following the spectral peaks helps to follow footprints of structures, but cannot provide insight to their evolution and interactions.

One of the major difficulties arising while studying the physical properties of large-scale coherent structures is that many of the findings can be biased by influences of smaller-scale structures and instabilities. This has led to an increasing interest in extracting the structures from the turbulent flows and to study their properties in the absence of small-scale structures. The latter, together with recent availability of large numerical and experimental datasets has led to increasing popularity of data driven methods.

After introduction of Proper Orthogonal Decomposition (POD) to fluid dynamics by Lumley (1967), numerous variations of this method were proposed building on the main idea which was to extract spatial and temporal flow structures from numerical and experimental data by decomposing the flow to spatially uncorrelated modes. This was particularly desirable as the largest amount of energy could be captured with the fewest number of modes, but also required the flow to be projected to orthogonal basis, hence removing the possibility for the modes to linearly interact. An example would be the study by Hellström and Smits (2014) who applied snapshots POD (Sirovich 1987) to cross-sectional PIV measurements, and found that the first 10 snapshots POD modes contribute 43% to average Reynolds shear stress and 15% to the kinetic energy. In a different approach, Dynamic Mode Decomposition (DMD) was introduced by Schmid and Sesterhenn (2008) decomposing the flow to correlated spatial modes possessing certain temporal frequencies and decay rates.

A majority of these methods decompose the flow on a stationary frame of reference leading to the need for large number of modes to describe the convecting features in the transport-dominated flows. This issue is addressed by several studies (Rowley and Marsden (2000) and Reiss et al. (2018)) introducing a spatial transformation in form of a shift. Sesterhenn and Shahirpour (2019) proposed a different approach by applying a spatio-temporal transformation in form of a rotation in space and time on a moving frame of reference along the characteristics of the flow. They observed a faster drop of singular values on a rotated frame compared to a shifted one.

In what follows we apply a CDMD to DNS data of turbulent pipe flow at $Re_\tau = 181$ with the objective of extracting a low dimensional subspace which mimics the main features of the flow such as Reynolds stress components, anisotropy invariant map and

axial velocity spectra. This offers a suitable basis for isolating the scales which are responsible for the spectral peaks (and will be the subject of a future study building up on the findings reported in this manuscript).

The flow under study only accommodates the energetic near-wall streaks where the larger outer layer structures have not emerged yet. This is confirmed by several studies showing that the LSMs and VLSMs emerge at $Re_\tau \geq 1500$ in pipe (Feldmann et al. 2018) and channel flow (Álamo and Jiménez 2003) where a more distinct scale separation will take place. Although the streaks possess smaller axial lengths scales compared to the other two groups of structures, in their absence at lower Reynolds numbers, streaks are the largest and the most energetic scales. Hence, they are referred to as large scales in this study to distinguish them from the smaller and less energetic scales.

2 Numerical Methods and Computational Details

The data used for the study is generated using an open-source, hybrid parallel DNS code (López et al. 2020). Hereby, Navier-Stokes equations are solved in cylindrical coordinates for an incompressible pipe flow fulfilling mass and momentum conservations given by

$$\nabla \cdot \mathbf{u} = 0\,, \quad \partial_t \mathbf{u} + \mathbf{u} \cdot \nabla \mathbf{u} = -\nabla p + \frac{1}{Re_b} \nabla^2 \mathbf{u}, \tag{1}$$

where $\mathbf{u}(\mathbf{x}, t)$ and $p(\mathbf{x}, t)$ represent velocity field (u, v, w) in cylindrical coordinates $\mathbf{x} = (x, r, \theta)$ and dynamic pressure respectively. No-slip boundary condition is applied at the walls together with periodic boundary condition for the inlet and outlet. The governing equations are solved for velocity and pressure, discretised with a combined Fourier-Galerkin / finite difference method in space and using a semi-implicit fractional-step of Hugues and Randriamampianina (1998), using second-order-accurate backwards differences and second order linear extrapolation for nonlinear term. More details on the numerical scheme can be found in the study by Shi et al. (2015). Simulations are carried out at bulk Reynolds number of $Re_b = 2RU_b/\nu = 5300$ for pipe length of $L = 50R$ with R, U_b and ν being respectively the pipe radius, bulk velocity and kinematic viscosity. The mentioned domain length has been chosen based on the study by Feldmann et al. (2018) which considers $L/R \geq 42$ to be sufficiently large to ensure that large-scale flow features are captured, fulfilling the requirement of capturing a minimum integral energy threshold of 2/3.

After the final grid refinement, calculations have been advanced for 400 convective time steps $t_c = R/U_b$, during which $CFL_{max} = 0.5$ was maintained, leading to simulation time step of $dt = 4.93 \times 10^{-4}\, t_c$. The grid spacing measured in wall units is chosen so that there are 5 and 20 points bellow $y^+ = 1$ and $y^+ = 10$ respectively, with the first point in the vicinity of the wall at $y^+ = 0.026$. The + superscript denotes normalisation by inner scaling using viscous length-scale ν/u_τ and friction velocity $u_\tau = \sqrt{\tau_w/\rho}$ where τ_w and ρ are the wall shear stress and density respectively. Further details on the simulation and grid spacing are mentioned in table 1. To ensure statistical convergence, the results are validated by comparing the statistical flow properties such as mean velocity and Reynolds stress components with benchmark DNS data in the next chapters.

Table 1 Details of the simulation and grid spacing. N_x, N_r, and N_θ are the number of grid points in (x, r, θ) directions and $Re_\tau = Ru_\tau/\nu$ is defined as shear Reynolds number

Re_τ	u_τ/U_b	$N_x \times N_r \times N_\theta$	(Δx^+)	$(\Delta r^+)_{min}$	$(\Delta r^+)_{max}$	$(\theta\Delta r^+)_{min}$	$(\theta\Delta r^+)_{max}$
181	0.068	$1800 \times 120 \times 286$	5	0.08	2.2	0.002	0.04

3 Methodology

Investigating transport-dominated phenomena on a stationary frame of reference adversely influences the observations. To remedy this issue, Sesterhenn and Shahirpour (2019) proposed a Characteristic DMD. The essence of a characteristic decomposition of the flow is to seek coherence as a persistent behaviour observed in space and time coupled together on a moving frame of reference, as opposed to spatial or temporal coherence individually. They introduced a transformation $\mathcal{T}$ in form of a rotation in space and time $\mathcal{T}(\mathbf{u}(x, r, \theta, t)) = \mathbf{u}(\xi, r, \theta, \tau)$ and used the drop of singular values as a measure of how well the convected phenomena can be described on each frame of reference. The algorithm is summarised in Fig. 1 where a rotation via three shears is implemented as proposed by Paeth (1990).

Two major advantages were presented for the spatio-temporal transformation. The first one is that convected phenomena could be described on the rotated frame with far fewer modes compared to a stationary frame. In addition, it was shown that singular values drop faster along the characteristics compared to those taken on a shifted moving frame which is obtained by a purely spatial transformation. The second advantage is that as expected, dynamics of the detected structures are captured more accurately.

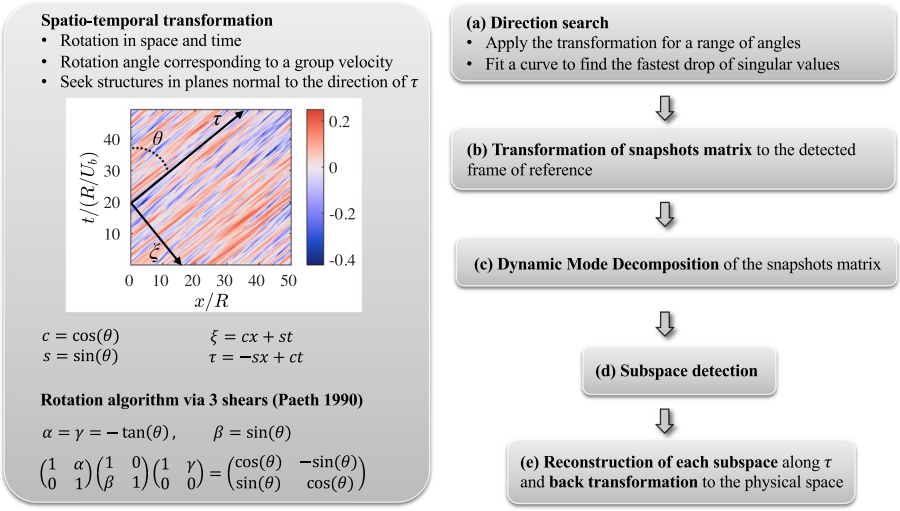

Fig. 1 CDMD algorithm (Sesterhenn and Shahirpour 2019) demonstrating the spatio-temporal rotation on a space-time diagram taken from DNS of pipe flow at wall normal distance of $y/R = 0.5$. Contours correspond to axial velocity perturbations normalised by bulk velocity

Having chosen the frame of reference, the decomposition method is selected based on the fact that the goal of this study is to analyse the interactions between the modes. We intend to present a framework in which the origins of structures, their regeneration mechanism, their sustainability and finally their decay process can be investigated. Therefore, the obtained eigen modes should be found such that they can give energy to other modes or to feed from them, and as a result, should not be forced to be normal to each other. To this end, the standard dynamic mode decomposition (Schmid 2010) has been taken as the main basis for decomposing the flow field. Three subsets of the modes are detected, reconstructed in spatio-temporal space and transformed back to physical space, where their contributions to Reynolds stress tensor and their anisotropy invariant maps are studied. Further details of the method can be found in the relevant manuscript (Sesterhenn and Shahirpour 2019).

A reference is needed to validate the identity of captured structures. What many studies have in common in their definition of coherent structures, is the footprint they leave behind in the Fourier space, in premultiplied energy spectra. Therefore, we verify our detected structures, by how well they represent the spectral peak and therefore, we use velocity field as the state vector in our analysis.

4 Results and Discussions

4.1 Detection of the Dominant Group Velocity

The main goal in the first step is to find the direction of characteristics along which the large-scale features of the flow can be described with fewest modes possible. The slope of the characteristics represents the group velocity u_g at which the most energetic large-scale features are being convected and is defined as the axial length-scale travelled per unit convective time defined as $t_c = R/U_b$.

Detecting structures on a moving frame of reference does not imply that a unique group velocity is assumed for different scales. Rather, it enables us to detect and describe different scales using a minimal number of modes (Sesterhenn and Shahirpour 2019). Each of the detected scales are travelling at group velocities close to that of the moving frame. Their group velocities are dependant on the axial and azimuthal wave number as well as the wall-normal location (Del Álamo and Jiménez 2009).

In Fig. 2, space-time diagram is shown for three velocity components at wall-normal location $y/R = 0.5$ for one azimuthal location. The colourmap represents the corresponding

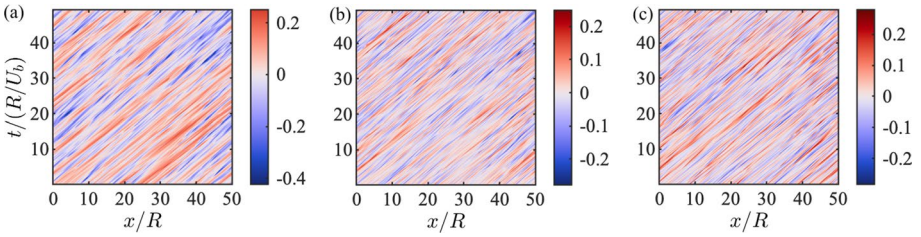

Fig. 2 Space-time diagrams for u **a**, v **b** and w **c** normalised by bulk velocity U_b at wall-normal location $y/R = 0.5$

velocity component normalised by bulk velocity. Although several group velocities can be observed for each component, one dominant group velocity can be perceived which corresponds to the energetic large-scale events. The dominant group velocity will get essentially smaller by moving closer to the wall and into the wall layer, and it will be larger in the outer layer and close to the pipe axis. A second observation is that the main group velocity appears to stay relatively constant for 50 t_c which is the time required to travel through the pipe once.

The objective is to decompose the flow into modes which describe the complete velocity field. Therefore, the direction along which the decomposition is applied should be chosen optimally for all velocity components. Optimality here is defined by detection of large-scale features using a minimal number of modes and is quantified by the drop of singular values along the characteristics. For each time-step the entire velocity field is stacked in one column vector which forms one of the columns of matrix $M_{(N_{ph} \times N_t)}$ with N_{ph} and N_t corresponding to the number of spatial points in physical space and time-steps respectively. The spatio-temporal rotation is then applied to M for a range of angles spaced 0.1 radian from each other. After each rotation, a singular value decomposition is carried out and the drop of singular values are recorded as shown in Fig. 3a. A piecewise cubic interpolation is then used to fit a curve to all the points and to find the maximum drop which is shown with a red marker for rotation angle of $\theta_g = 1.311$ corresponding to group velocity of $u_g = 1.06\, U_b = 15.5\, u_\tau$. This group velocity is equal to the mean radial velocity found at wall-normal location $y^+ = 1 - (r/R)^+ = 44$. In Fig. 3b, u_g is annotated along with the mean radial velocity profile compared with the benchmark data by El Khoury et al. (2013). By rotating the matrix M by θ_g, the data will be transformed to a moving frame of reference with the direction of characteristics serving as the new time coordinate. We search for coherent structures in planes normal to the characteristics as they travel in space and time and undergo minimal changes while maintaining their coherence.

4.2 Decomposition and Subspace Detection

Having detected the optimal group velocity, matrix M is formed using 500 timesteps with spatial resolution of $(900 \times 60 \times 143)$ in (x, r, θ) directions. To ensure that the dynamics of the modes are captured correctly, timestep of $dt_{\text{CDMD}} = 0.2\, t_c$ is chosen between the columns of M. Therefore, each event moving at U_b propagates two times through the entire

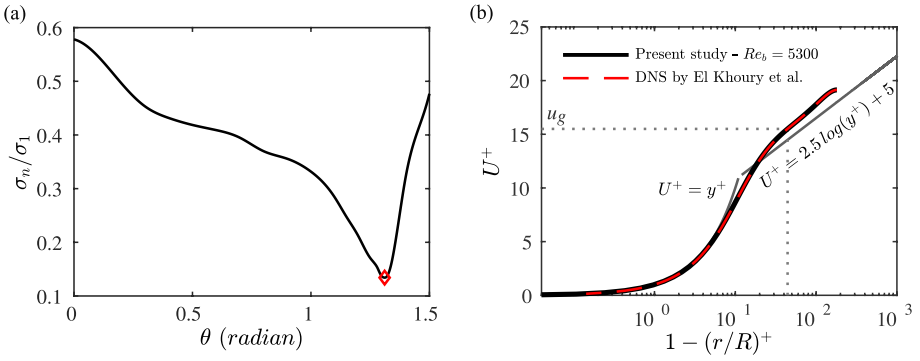

Fig. 3 Drop of singular values for a range of rotation angles **a** and mean radial velocity profile compared against the benchmark data **b**

pipe. Transforming the data to spatio-temporal space and choosing the largest $\xi - \tau$ window in the rotated frame of reference results in the snapshots matrix in spatio-temporal space $X_{st} = \mathcal{T}(M)$, with $N_\xi = 290$ and $N_\tau = 843$ points along ξ and τ respectively. A standard DMD is carried out to decompose X_{st} into the dynamic modes $\boldsymbol{\phi}_i$ and their corresponding coefficients $c_i(\tau)$ such that $X_{st} = \boldsymbol{\Phi} C$ where $\boldsymbol{\Phi}$ and C are matrices of dynamic modes and their coefficients for all timesteps. Continuous-time eigenvalues are transformed back to physical space with their real and imaginary parts representing decay rates and frequencies of the modes respectively in physical time. In Fig. 4, time averaged mode coefficients normalised by their $\mathcal{L}_2$ norm, dimensionless decay rates $\hat{d} = d/(U_b/R)$ and frequencies $\hat{f} = f/(U_b/R)$ are plotted with the modes being sorted by their decay rates. All the frequencies in spatio-temporal space are within the range of $0 \leq \hat{f}_{st} < 2.5$ which corresponds to $0 \leq \hat{f} < 10$ after transformation to physical space.

Next, a subset of modes is to be selected constituting a subspace (subspace I) to fulfil certain criteria which are chosen with the knowledge that for turbulent pipe flow at this Reynolds number, there exists only one peak in the premultiplied energy spectra. The first criteria is that subspace I should accommodate energetic structures with large spatio-temporal length-scales. Therefore, it is expected to have a large contribution to the spectral peak which is known as the footprint of large-scale structures in premultiplied energy spectra. Given the nature of coherent structures, the second criteria dictates that the modes in this subspace should not possess large decay rates. This is to ensure that energetic modes with short lifetimes will not be a member of this subspace. Similarly, the candidate modes are expected to have small frequencies and not undergo strong oscillations.

We hypothesize that the modes fulfilling the mentioned criteria are expected to possess another significant property. Due to the spatio-temporal coherence of the flow captured by these modes, they are expected to have major interactions with each other, but have smaller interactions with the rest of the modes. We define this interaction in terms

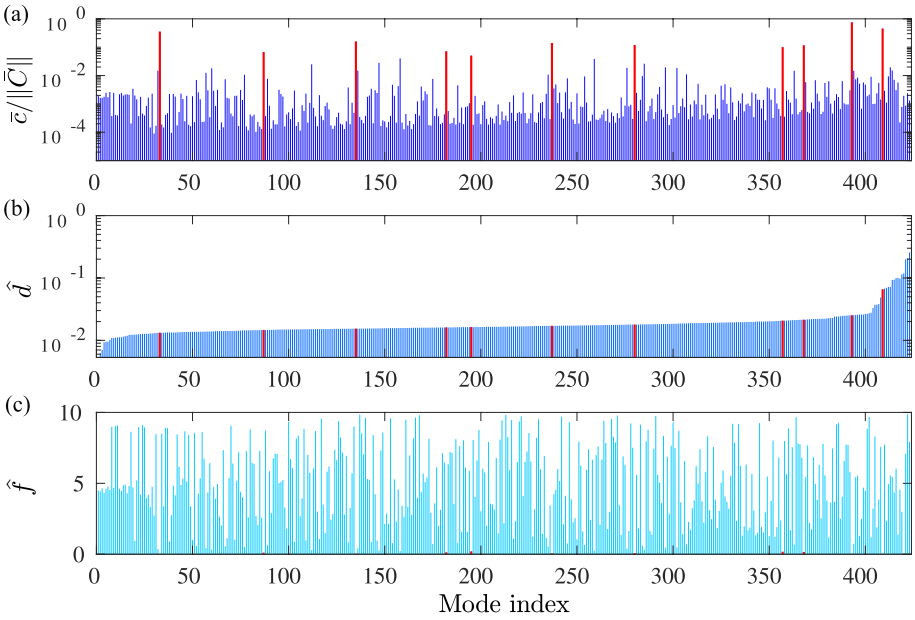

Fig. 4 Dynamic mode amplitudes, decay rates and frequencies

of the angle between the modes as well as the energy which is gained or lost by the flow as a result of presence of each two modes in a subspace. This implies that the modes in subspace I, besides being energetic, should have small angles between each other and large ones with the remaining modes.

To calculate the energy of a subspace, we first consider subspace S comprised of two modes $S = \{\boldsymbol{\phi}_1, \boldsymbol{\phi}_2\}$ and coefficients matrix C_S with rows defined as $c_1(\tau)$ and $c_2(\tau)$ that can be used to obtain $X_S = SC_S$. Columns of X_S and C_S can be used to write for each timestep $\chi_S(\tau) = S\boldsymbol{c}_S(\tau) = \boldsymbol{\phi}_1 c_1(\tau) + \boldsymbol{\phi}_2 c_2(\tau)$. The total energy of S integrated along τ is then defined by

$$E_S = \sum_{\tau=1}^{N_\tau} \boldsymbol{c}_S^*(\tau)\, S^* S\, \boldsymbol{c}_S(\tau), \tag{2}$$

and energy of S can be written for each time step τ as

$$\begin{aligned} E_S(\tau) &= \chi_S^*(\tau)\chi_S(\tau) = \boldsymbol{c}_S^*(\tau)\, S^* S\, \boldsymbol{c}_S(\tau) = \Big(c_1^*(\tau)\boldsymbol{\phi}_1^* + c_2^*(\tau)\boldsymbol{\phi}_2^*\Big)\Big(\boldsymbol{\phi}_1 c_1(\tau) + \boldsymbol{\phi}_2 c_2(\tau)\Big) \\ &= \underbrace{c_1^*(\tau)\boldsymbol{\phi}_1^*\boldsymbol{\phi}_1 c_1(\tau)}_{E_1(\tau)} + \underbrace{c_1^*(\tau)\boldsymbol{\phi}_1^*\boldsymbol{\phi}_2 c_2(\tau) + c_2^*(\tau)\boldsymbol{\phi}_2^*\boldsymbol{\phi}_1 c_1(\tau)}_{E_{1|2}(\tau)} + \underbrace{c_2^*(\tau)\boldsymbol{\phi}_2^*\boldsymbol{\phi}_2 c_2(\tau)}_{E_2(\tau)}, \end{aligned} \tag{3}$$

where the terms $E_1(\tau)$ and $E_2(\tau)$ in Eq. 3 correspond to the energy of modes $\boldsymbol{\phi}_1$ and $\boldsymbol{\phi}_2$ respectively at one timestep.

The term $E_{1|2}(\tau)$ represents the energy added to or taken from X_s as a result of superposition of $\boldsymbol{\phi}_1$ and $\boldsymbol{\phi}_2$. Coexistence of two non-orthogonal modes (or subspaces) leads to interactions between them which can be studied in terms of their kinematic and dynamic properties. The former corresponds to how the net result of their interaction influences for instance the kinetic energy and other turbulent properties of X_s. The latter on the other hand focuses on the temporal evolution of the interaction and quantifies how presence of each mode influences the role of the other in time. In this study we are mainly investigating the kinematics of subspace interactions (referred to 'interactions' from here on out) and their dynamics are the subject of a future study.

For modes that are orthogonal to each other, the term $E_{1|2}$ vanishes and for mode pairs with small angles, $E_{1|2}$ can have large positive or negative values. Equation 3 can be generalised to the case where $\boldsymbol{\phi}_1$ and $\boldsymbol{\phi}_2$ are each a subspace.

To detect a subspace I_n with n most energetic modes that represents the full field energy with fewest number of modes, and to observe how the subspace energy changes as the next energetic mode is added to it, cumulative energy is calculated for the first n dominant modes, integrated along τ and normalised by the total energy as

$$\gamma_{I_n} = E_{I_n}/E_{\boldsymbol{\Phi}}. \tag{4}$$

and plotted in Fig. 5a for the first 50 modes. E_{I_n} represents energy of subspace I possessing n modes integrated over time. A fast drop is observed for the first few modes added, where two minima are observed for 4 and 6 modes resulting in subspace energy close to 1. ($\gamma_{I_4} = 1.1$ and $\gamma_{I_6} = 0.9$). Adding more modes increases the energy, but finally by having 11 modes, subspace energy will drop again to $\gamma_{I_{11}} = 0.9$. It is clear that adding the next modes makes only minimal changes in the subspace energy.

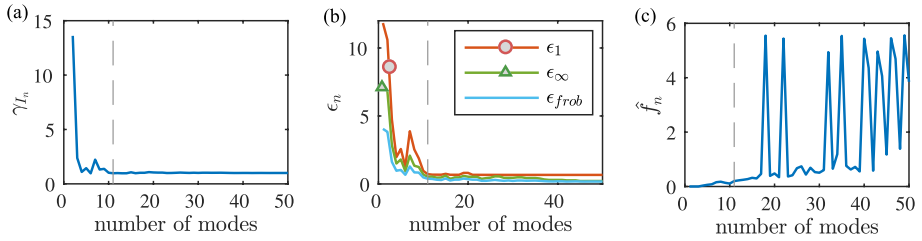

Fig. 5 Cumulative energy **a**, relative error **b** and frequencies **c** of the first n dominant modes

Next, relative error is calculated for reconstruction of modes in subspace I_n having n modes with the corresponding coefficients matrix C_{I_n} (Eq. 5). Three matrix norms have been used with $p = \{1, \infty, F\}$ for one-norm, infinity norm and frobenius norm respectively.

$$\epsilon_n = \|X - I_n C_{I_n}\|_p / \|X\|_p. \tag{5}$$

As shown in Fig. 5b, all relative errors reach two minima for 4 and 6 modes, increase for 7 modes, and then drop strongly for 11 modes while minimally changing beyond that point. As depicted in Fig. 5c, these 11 modes have very small frequencies compared to the rest of the modes.

The candidate 11 modes are highlighted in red in Fig. 4 with red bars. They have a small mean decay rate of $\hat{d}_I = 0.022$ and undergo minimal oscillations with average frequency of $\hat{f}_I = 0.086$ in the range of $0 \leq \hat{f} \leq 0.2$. All the remaining modes oscillate with larger frequencies $0.22 \leq \hat{f} \leq 9.86$ with the exception of mode 420 which has a large decay rate and small amplitude and therefore does not meet the criteria to be part of this subspace. 8 of the candidate modes have large amplitudes $\bar{c}/\|\bar{C}\| \geq 0.1$ and the rest, in spite of having smaller amplitudes $0.05 \leq \bar{c}/\|\bar{C}\| \leq 0.07$, still possess much smaller frequencies compared to the rest of the modes. Therefore, based on the cumulative energy of subspace I, its relative error, mode amplitudes, their decay rates and frequencies, the first 11 dominant modes are chosen as members of subspace I.

Having detected a subset of energetic modes matching the mentioned criteria, we verify orthogonality of each member of this subset to modes residing inside and outside the subset. Mode-pair angles $m_{33}\angle m_i$ are plotted as an example in Fig. 6a with blue markers showing the angles that mode 33 (one of the members of subspace I) makes with all the other

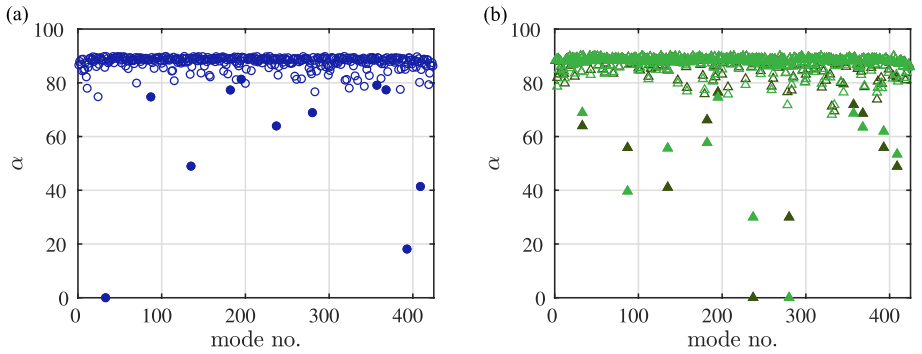

Fig. 6 Angles between mode-pairs $m_{33}\angle m_i$ **a**, $m_{237}\angle m_i$ and $m_{280}\angle m_i$ **b**

modes. Filled blue markers, correspond to subspace I members. It is readily seen that majority of the modes outside subspace I, are almost orthogonal to mode 33 as they accumulate close to $\alpha = 90$. On the other hand, the smallest angles are made with members of subspace I (m_{393} and m_{409}), indicating interaction between m_{33} with a small decay rate, with two modes with rather larger decay rates. In Fig. 6b, mode pair angles $m_{237}\angle m_i$ and $m_{280}\angle m_i$ are plotted. Here it is also observed that modes outside subspace I are mostly orthogonal to m_{237} and m_{280}. These two modes appear to make small angles with one another and rather larger angles with the rest of the modes in subspace I. A similar behaviour exists for all the modes in subspace I.

A small angle between two modes, provides the potential for a large energy interaction. But as inferred from Eq. 3, the term $E_{1|2}$ is dependant also on the mode coefficients besides the inner product of the two modes. Therefore in the next step, integrated energy interactions $\hat{E}_{i|k}$ are calculated between each mode (k) in subspace I and all the other modes (i) normalised by the total energy of the flow (with $\hat{\cdot}$ denoting the normalisation). The results are plotted for $\hat{E}_{i|237}$ in Fig. 7a with circles and diamond markers corresponding to positive and negative values respectively. Filled markers represent modes in subspace I, which show clearly the largest interactions with m_{237}, some with positive and some with negative values. Apart from the contributions of the modes in subspace I (filled markers), two distinct regions also appear in this plot. A smaller number of modes can be seen at $\hat{E}_{i|237} \geq 10^{-3}$ and majority of them seem to be accumulated below this limit. This implies that there are certain modes outside subspace I, which are interacting more than the rest with m_{237}. These two regions appear for all the modes in subspace I indicating emergence of a second subspace, whose members are chosen based on how much energy they bring or take from the flow while interacting with subspace I. To detect the modes fitting in the new subspace, the term $\hat{E}_{i|I}$ should be calculated for all the members of subspace I as

$$\hat{E}_{i|I} = \frac{\sum_{\tau=1}^{N_\tau} \sum_{k=1}^{N_I} \left(c_i^*(\tau)\, \boldsymbol{\phi}_i^* \boldsymbol{\phi}_k\, c_k(\tau) + c_k^*(\tau)\, \boldsymbol{\phi}_k^* \boldsymbol{\phi}_i\, c_i(\tau) \right)}{\sum_{\tau=1}^{N_\tau} \boldsymbol{c}^*(\tau)\, \boldsymbol{\Phi}^* \boldsymbol{\Phi}\, \boldsymbol{c}(\tau)}, \tag{6}$$

with N_τ and N_I being the total number of modes and the number of modes in subspace I respectively. The vector calculated using Eq. 6 is sorted in a descending order and modes

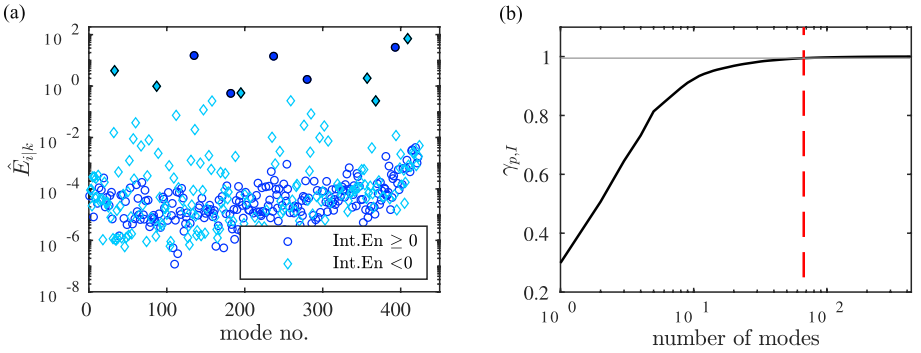

Fig. 7 Normalised energy interactions between mode m_{237} (a member of Sub I) and all the other modes **a**, and cumulative energy interaction between subspace I and the rest of the modes **b**

in subspace I are excluded from the set in order to detect the largest contributions to subspace I. Cumulative energy interaction is then given for the first p dominant contributions by

$$\gamma_{p,I} = \frac{\sum_{j=1}^{p} \hat{E}_{j|I}}{\sum_{j=1}^{N_\tau - N_I} \hat{E}_{j|I}}, \tag{7}$$

and is plotted in Fig. 7b. Cumulative energy contribution rises rapidly with the first 10 modes and reaches a saturation point after 60 modes, beyond which the energy does not change much by adding the remaining modes. Taking 67 modes, where a red dashed line is plotted, captures 98% of the total contribution (grey solid line).

Having detected a second subspace, the remaining modes are grouped together to form the third subspace. Subspaces I, II and III each with 11, 67 and 346 modes amount to 3%, 15% and 82% of the total number of modes respectively. Their total kinetic energy is calculated using Eq. 2 being equal to 97%, 15% and 2% of the snapshots energy for the first, second and third subspaces respectively. Subspace interactions I | II and II | III lead to 12% and 2% energy loss, whereas interactions between the first and third subspaces does not cause any overall energy gain or loss.

To demonstrate a comparison with decompositions on a stationary frame of reference, the two following studies are considered. Hellström and Smits (2014) show for example that the first 10 snapshots POD modes represent 14% and 15% of the energy for $Re_D = 47000$ and $Re_D = 93000$ with Re_D being the Reynolds number based on the centreline velocity. Covering a wider range of Reynolds numbers, Yu et al. (2022) apply a Fourier decompositions in the azimuthal direction and a POD in the radial direction at $180 \leq Re_\tau \leq 6000$. The cumulative energy of the first POD mode associated with the first 10 azimuthal modes amounts approximately to 33% and 40% for shears Reynolds numbers of 180 and 6000 respectively. Their first, third and fifth POD modes contribute respectively 60%, 80% and 90% to the energy of the azimuthal modes at $Re_\tau = 6000$.

In the next step, each of the detected subspaces are reconstructed along τ. To have a visual comparison between the full field and the subspaces, space-time diagrams are plotted for axial velocity components in Fig. 8 at wall-normal location $y = 0.34R$ ($y^+ = 61.5$) for one azimuthal location. Comparing the full field with Subspace I in Fig. 8a and b, it can be seen that the large-scale flow patterns are present very well in spite of the fact that only 3% of the modes exist in this subspace. Magnitudes of negative and positive perturbations agree well with those of the full field. Small-scale patterns are clearly missing from the reconstruction as expected. Dominant structures in this subspace appear to remain stationary along the direction of τ.

Subspace II in Fig. 8c accommodates small-scale patterns with perturbations which are considerably less energetic than those captured in subspace I. Oblique patterns emerging show that structures here have different group velocities compared to the dominant one. Some appear to move backwards relative to the moving frame of reference indicating a slower convection velocity, whereas others move forward at higher velocity. Absence of strong vertical patterns in this figure shows that no energetic structure moving with the dominant group velocity is present in subspace II.

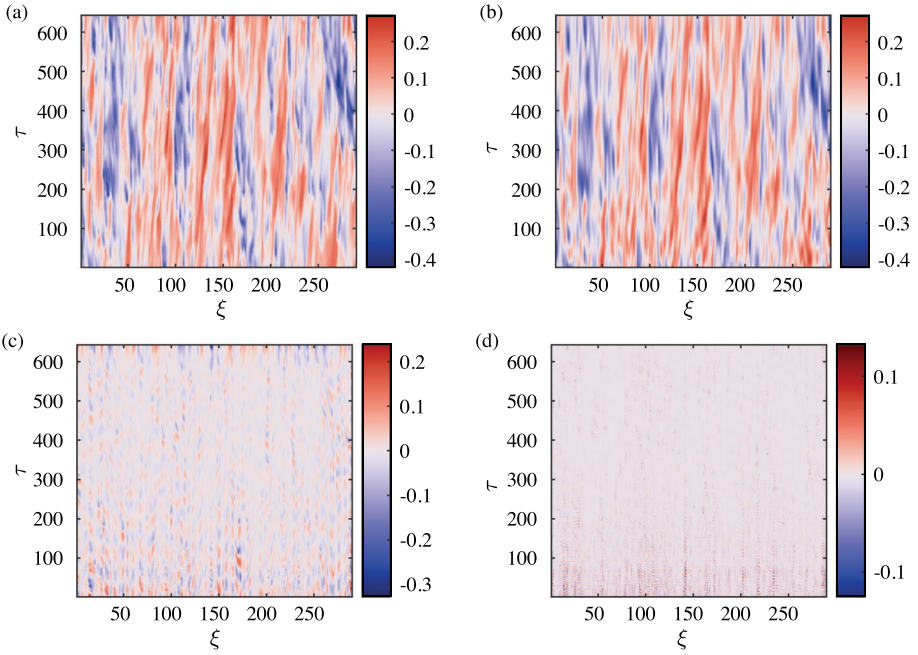

Fig. 8 Space-time diagram in spatio-temporal space for the full field **a** and subspaces I **b**, II **c** and III **d**, at wall-normal location $y = 0.34R$ and one azimuthal point

Subspace III with 82% of the modes bears traces of some small-scale patterns similar to those in subspace II, but is mainly populated with very small-scale structures. No dominant group velocity is observable in this subspace.

4.3 Subspaces in Physical Space

Each reconstructed subspace is transformed back to physical space. In Fig. 9, iso-surfaces of streamwise velocity component are shown for the full field (Fig. 9a) and for each subspace. Similar to what was seen in the spacetime diagram, the structures in subspace I (Fig. 9b) appear to be similar to those in full filed. This resemblance is observed in terms of where high and low momentum regions are located and also in terms of amplitudes of perturbations (In both subfigures iso-levels $u = \pm 0.1\, U_b$ are plotted). Axial length-scales in both figures perceived from the large-scale structures agree well and they will be examined in the next chapters in premultiplied velocity spectra.

Subspace II in Fig. 9c on the other hand, accommodates only smaller scale structures with lower perturbation magnitudes (with iso-levels $u = \pm 0.04\, U_b$). The modes in this subspace were chosen based on the level of their interactions with subspace I causing large energy gains or losses. On the other hand it was shown in Fig. 5 that the total energy of the flow will not change drastically beyond 11 modes. This implies that although the two subspaces have large energy interactions, the overall energy of subspace I remains relatively constant. Subspace III is plotted with iso-levels $u = \pm 0.005\, U_b$ with two major length-scales being present in the flow, both of which are smaller than those present in the other subspaces.

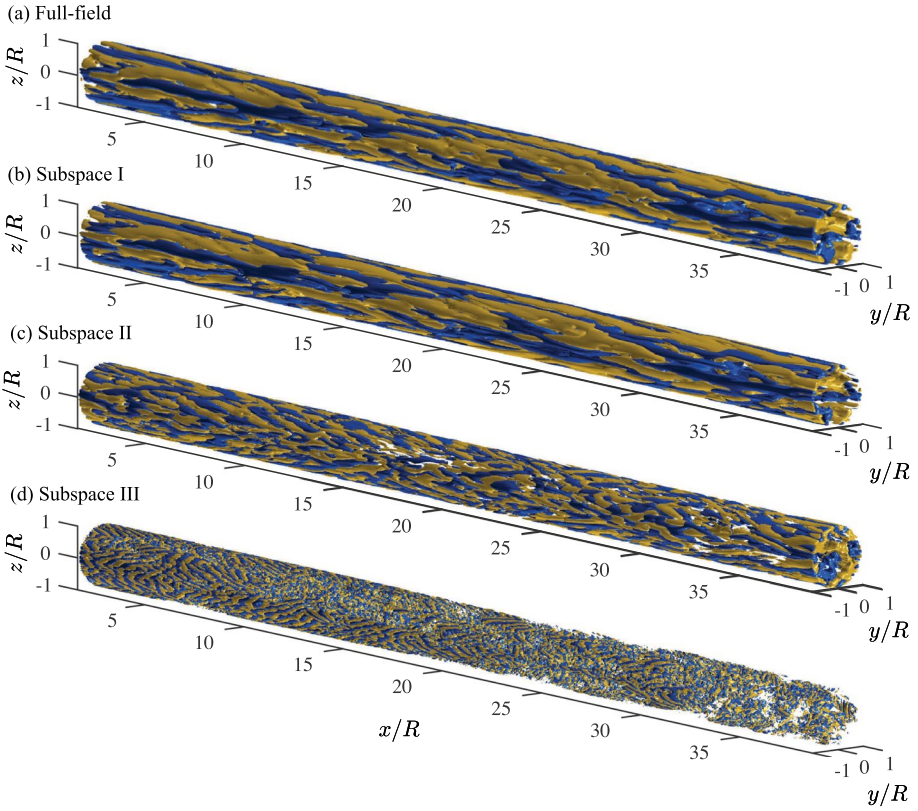

Fig. 9 Iso-surfaces of axial velocity component of the full field compared against each subspace. Iso-levels for the full field **a** and subspace I **b** are identical with yellow and blue corresponding to $u = \pm 0.1\, U_b$. In subfigures **c** and **d** iso-levels of $u = \pm 0.04\, U_b$ and $\pm 0.005\, U_b$ are plotted respectively for subspaces II and III

4.4 limitations and Constraints

The statistical turbulence properties of the full field diverge from those of the snapshots matrix in physical space $X_{ph} = \mathcal{T}^{-1}(X_{st})$. The first reason is that in order for the second order statistics to converge, 4000 data realisations recorded for 400 convective timesteps have been used, whereas taking the same number of timesteps for DMD was not possible due to memory limitations. The second reason is the linear interpolation used for the spatio-temporal transformations.

The first limitation could be only partially removed using a streaming DMD (Hemati et al. 2014) and at the expense of truncating the singular values. As in this study it was intended to keep all non-zero singular values, a streaming DMD was not used. Employing higher order interpolation schemes and using larger number of timesteps, substantially increase the computation time specially at higher Reynolds numbers. It was also observed that the present setup does not bias the conclusions. Therefore, turbulence properties of the subspaces in subchapters 4.5 and 4.8 are presented using three references. The first two references are the full field and DNS data by El Khoury et al. (2013)

which are compared against each other to validate the simulation results. X_{ph} serves as the third reference against which the subspaces are compared. In subchapter 4.6, the difference between the length scales in snapshots and the full field is compensated by applying the same correction to the snapshots and all subspaces.

4.5 Contribution to Reynolds Stress Tensor

Contributions of each subspace to components of Reynolds stress tensor are calculated in physical space and are compared against the snapshots X_{ph} (plotted in black dashed lines), the full field (plotted in grey solid lines) and the benchmark data (plotted in red dotted lines) in Fig. 10. This helps to verify whether the differences between subspace statistics and the full field, are a result of the constraints mentioned in chapter 4.4, or a property of the flow represented by the corresponding subspace. The invariants of Reynolds stress tensor are also calculated for each subspace to provide a measure of how the entire tensor compares with that of the snapshots. The first invariant being equal to the turbulent kinetic energy is already reported in the previous chapter for each subspace. The remaining two are presented in this chapter.

To ensure the accuracy and reliability of the simulated data, Reynolds stress components of the full filed are plotted in grey solid lines and are compared against the benchmark

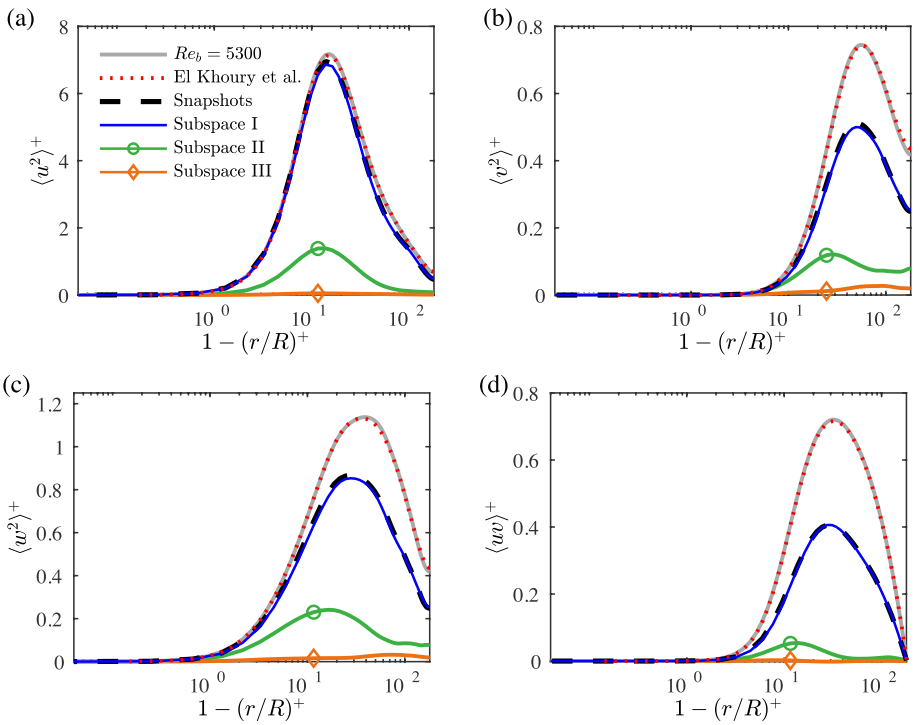

Fig. 10 Reynolds stress components of the full field (grey solid lines) compared against those of the benchmark data (red dashed lines), each subspace (coloured solid lines) and the snapshots matrix (black dashed line). Black and blue lines collapse very well in all figures which indicates a very large contribution of sI to Reynolds stress components

DNS data by El Khoury et al. (2013) plotted in red dotted lines in Fig. 10. Stress tensor components of the full field agree very well with those of the benchmark with the peaks being located at $y^+ = [15, 56, 36, 32]$ for $\langle u^2 \rangle$, $\langle v^2 \rangle$, $\langle w^2 \rangle$ and $\langle uv \rangle$ respectively.

Subspace I (sI) (plotted in solid blue lines), shows substantial contributions to the stress components of the snapshots (plotted in dashed black lines) with average contribution of 98%. The wall-normal locations of the peaks coincide with those of the snapshots at $y^+ = [14, 50, 28, 28]$ for $\langle u^2 \rangle$, $\langle v^2 \rangle$, $\langle w^2 \rangle$ and $\langle uv \rangle$. The second and third stress tensor invariants of this subspace amount to 97% and 96% of those of the snapshots.

Subspace II which appears with axial length-scales smaller than sI and larger than sIII (Fig. 9) is plotted in green solid lines. It contributes most to the radial stress component (22%) and least to the axial-radial one (6%) reaching the peak values at wall-normal locations $y^+ = 28$ and $y^+ = 14$ respectively. The peaks of axial and azimuthal components occur at $y^+ = 14$ and $y^+ = 16$ with 14% and 21% contributions to the corresponding components of snapshots. Except for the axial component, all the peaks in this subspace have moved clearly closer to the wall compared to the snapshots. The second and third invariants of the stress tensor of this subspace are equal to 2% and 0.4% of those of the snapshots respectively.

Subspace III accommodating very small scale structures and represented by 82% of the modes has 3.3% average contribution to the diagonal Reynolds stress components and 0.1% to $\langle uv \rangle$ reaching their maxima at $y^+ = [12, 92, 74, 31]$ respectively. This subspace contributes less than 0.02% to the second and third invariants of stress tensor.

We emphasise that the success measure of the method is how well Reynolds stress components in subspace I (plotted in solid blue lines) collapse with those of the snapshots (plotted in dashed black lines). The divergence of snapshots from the full field is caused by the constraints mentioned in chapter 4.4.

While the sum of three subspaces gives the snapshots (sI + sII + sIII = X_{ph}), the sum of stress components of all three subspaces in Fig. 10 clearly does not amount to those of the snapshots ($\langle u^2 \rangle_{\mathrm{sI}} + \langle u^2 \rangle_{\mathrm{sII}} + \langle u^2 \rangle_{\mathrm{sIII}} \neq \langle u^2 \rangle_{X_{ph}}$). This is due to the fact that the subspaces are not orthogonal to each other and therefore their inner products are non-zero. This implies that their coexistence leads to interactions which result in either adding or removing energy from the flow. To quantify the net impact of subspace interactions on the Reynolds stress components, $\langle u^2 \rangle$ and $\langle uv \rangle$ are written for subspace $S = \{\boldsymbol{\phi}_1, \boldsymbol{\phi}_2\}$ as

$$\langle u_S^2 \rangle = \langle u_{\phi_1}^2 \rangle + \langle u_{\phi_2}^2 \rangle + \underbrace{\langle 2\, u_{\phi_1}\, u_{\phi_2} \rangle}_{\langle u^2 \rangle_{\phi_1|\phi_2}}, \tag{8}$$

$$\langle u_S\, v_S \rangle = \langle u_{\phi_1} v_{\phi_1} \rangle + \langle u_{\phi_2} v_{\phi_2} \rangle + \underbrace{\langle u_{\phi_1} v_{\phi_2} + u_{\phi_2} v_{\phi_1} \rangle}_{\langle uv \rangle_{\phi_1|\phi_2}}. \tag{9}$$

Equations 8 and 9 can be generalised to the case where ϕ_1 and ϕ_2 are each a subspace. For the case that subspace S is comprised of more modes, the inner products should be calculated for each mode pair accordingly. Similar to what was shown for the energy of subspaces, it can be seen here that subspace interactions results in non-zero values for the terms $\langle u^2 \rangle_{\phi_1|\phi_2}$ and $\langle uv \rangle_{\phi_1|\phi_2}$. By extending Eq. 8 to the three subspaces, the following will be valid

$$\langle u^2\rangle_{\mathrm{sI}} + \langle u^2\rangle_{\mathrm{sII}} + \langle u^2\rangle_{\mathrm{sIII}} + \langle u^2\rangle_{\mathrm{sI|sII}} + \langle u^2\rangle_{\mathrm{sII|sIII}} + \langle u^2\rangle_{\mathrm{sI|sIII}} = \langle u^2\rangle_{X_{ph}}. \tag{10}$$

These terms are calculated for each subspace pair and plotted in Fig. 11 along with the Reynolds stress components of each subspace. Figures are zoomed to highlight each curve. It can be seen for all diagonal components, that while the three subspaces acquire positive values for all wall normal locations, their interactions have negative values. The same observation is valid for $\langle uv\rangle$ component in subspaces I and II, whereas subspace III becomes slightly negative in the outer layer.

A second observation which is valid in all components is that sII and sI|sII exhibit very similar behaviours with opposite signs. This implies that the contribution of subspace sII is almost entirely compensated by its interactions with sI. While a similar behaviour can be seen for subspace III and its interaction with sII, sI|sIII term is close to zero for all wall-normal locations.

4.6 Energy Spectra

The energy content of each length-scale is analysed for each subspace using premultiplied streamwise spectra of velocity auto correlations ($\varphi_{uu}, \varphi_{vv}, \varphi_{ww}$) and cross correlation (φ_{uv}) plotted in Fig. 12 for the snapshots in coloured contours and black contour lines. Blue, green and orange dashed contour levels represent subspaces I, II and III respectively. All the spectra have been normalised by the variance of the corresponding velocity component

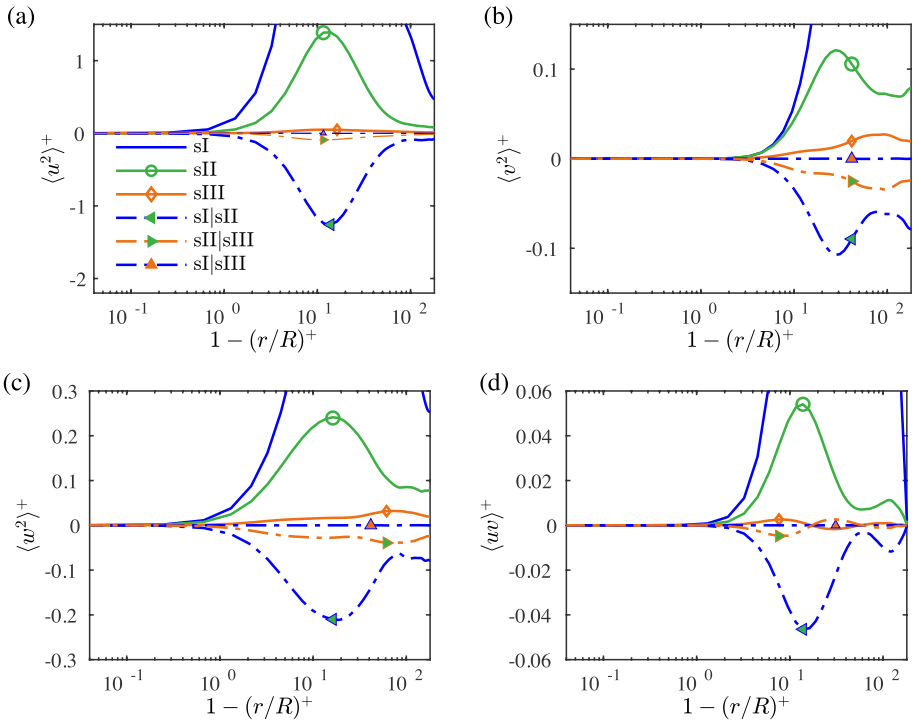

Fig. 11 Reynolds stress components of each subspace (coloured solid lines) and the net impact of their interactions on the Reynolds stresses (dash dotted lines)

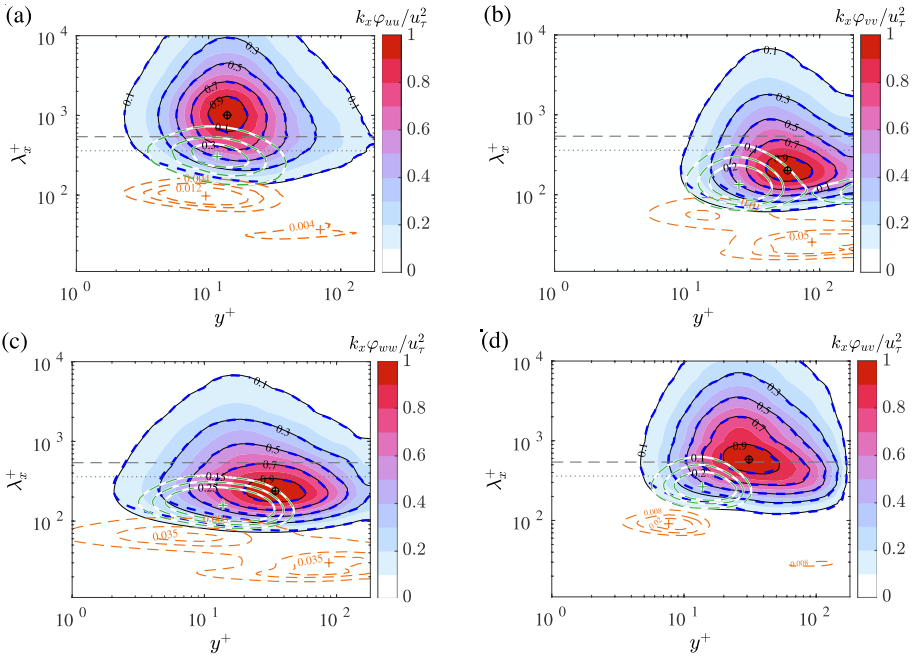

Fig. 12 Premultiplied spectra of velocity auto correlations φ_{uu} **a**, φ_{vv} **b**, φ_{ww} **c** and cross correlation φ_{uv} **d**. Coloured contours and solid black lines correspond to the snapshots. Subspaces sI, sII and sIII are plotted in blue, green and orange dashed lines respectively. Dotted and dashed grey lines represent the wave lengths $\lambda_x = 2R$ and $3R$ respectively. All the spectra have been normalised by the variance of the corresponding velocity component and by the peak value in the snapshots spectra

and by the peak value in the snapshots spectra. Blue dashed lines and black solid contour lines correspond to the same levels annotated in black. Black circle and plus markers indicate spectral peaks of the snapshots and subspace I. Coloured plus markers point to the peak locations of the corresponding subspace. The horizontal dotted and dashed lines are plotted as a reference for the commonly accepted axial length-scales of LSMs at $\lambda_x = 2R$ and $3R$ respectively. Inspecting the axial spectra of the full field shows that scales with energy levels larger than 30% of the spectral peak have been captured completely, whereas for radial and azimuthal spectra this corresponds to 10% of the spectral peaks.

In the spectra of axial velocity in Fig. 12a, all large-scale structures are captured in subspace I and maximum energy is found for wave-length $\lambda^+ = 1006$ at $y^+ = 13.8$. Smaller structures with up to length-scale of $\lambda^+ = 300$ are also present in this subspace. Energy of wave-lengths $\lambda^+ \leq 300$ drop compared to the snapshots at $3 \leq y^+ \leq 30$, where the solid black levels diverge from the dashed blue ones. Subspaces II and III appear with spectral peaks having smaller axial length-scales of $\lambda^+ = 304$ and 97 at $y^+ = 11.6$ and 9.5 with normalised peak energy of 0.37 and 0.02 respectively.

The radial velocity component has the shortest axial wave-length compared to the other two components as seen in Fig. 12b with the main peak occurring at $y^+ = 57$ for $\lambda^+ = 201$ for the snapshots and sI. The peaks of subspaces II and III emerge with smaller wave-lengths of $\lambda^+ = 134$ and 25 at $y^+ = 24$ and 87 with normalised peak energy of 0.3 and 0.084 respectively. What can be observed in all subplots of Fig. 12, is that the spectral

peaks found for subspace I coincide with those in the snapshots, in terms of their wall-normal locations and axial wave-lengths, with their energy content peaking on average at 99% of the snapshots spectral peaks. Subspace I has captured large-scale energetic structures, and where its energy diverges from the snapshots, the next subspaces emerge with a peak. Spectral peaks in subspace II show a strong shift to the vicinity of the wall, although the shift is smaller for $k_x\varphi_{uu}$. Subspace III appears in all spectral maps with two low energy peaks, one below the main peak closer to the wall and one above it, with length-scales $\lambda^+ \leq 100$. The more energetic peak belongs to the one with larger wave-length for φ_{uu} and φ_{uv}, whereas for φ_{vv} and φ_{ww} it represents the smaller wave-length.

Given the low Reynolds number investigated in this study, outer flow structures such as LSMs and VLSMs are not formed. The only present structures are the large-scale streaks whose wall-normal locations and axial wave-lengths match those of the spectral peaks in Fig. 12. It can bee seen that the streaks have been captured in subspace I together with smaller scale structures which are persistent in time. This shows that subspace I represents the spectral footprint of the flow with a high accuracy using only 3% of the total modes.

4.7 Interactions in Fourier Space

Spectral interactions between the detected subspaces are studied in Fourier space. Superposition of non-orthogonal modes belonging to different subspaces will lead to addition or extraction of energy from the flow. To quantify this energy and track the scales responsible for it, velocity spectrum $(\varphi_{uu})_S$ of subspace $S = \{\phi_1, \phi_2\}$ is written for the streamwise fluctuations as

$$(\varphi_{uu})_S = \underbrace{\hat{u}^*_{\phi_1}.\hat{u}_{\phi_1}}_{(\varphi_{uu})\phi_1} + \underbrace{\hat{u}^*_{\phi_2}.\hat{u}_{\phi_2}}_{(\varphi_{uu})\phi_2} + \underbrace{\hat{u}^*_{\phi_1}.\hat{u}_{\phi_2} + \hat{u}^*_{\phi_2}.\hat{u}_{\phi_1}}_{(\varphi_{uu})\phi_1|\phi_2} \tag{11}$$

where $\hat{u}$ represents the Fourier transform of u. The last term in this equation, being the inner product of the two subspaces in Fourier space, quantifies the energy content per wave number added or extracted from the flow, and highlights the wave numbers at which the latter takes place. A similar equation can be written for spectra of velocity cross-correlation $(\varphi_{uv})_S$ where the inner product is written between streamwise component of one subspace and the radial component of the other.

$$(\varphi_{uv})_S = \underbrace{\hat{u}^*_{\phi_1}.\hat{v}_{\phi_1}}_{(\varphi_{uv})\phi_1} + \underbrace{\hat{u}^*_{\phi_2}.\hat{v}_{\phi_2}}_{(\varphi_{uv})\phi_2} + \underbrace{\hat{u}^*_{\phi_1}.\hat{v}_{\phi_2} + \hat{u}^*_{\phi_2}.\hat{v}_{\phi_1}}_{(\varphi_{uv})\phi_1|\phi_2} \tag{12}$$

These equations can be generalised for the case where each of the constituent modes are a subspace. The relevant terms are then computed for the three detected subspaces and the results are depicted in Fig. 13. Interactions sI|sII, sII|sIII and sI|sIII are plotted respectively in blue, green and orange dashed lines. Coloured contours of the snapshots are also plotted as a reference. In all the spectral maps, sI|sII and sII|sIII terms show negative values whereas the sI|sIII term has very small but positive values.

In the spectra of *uu*, a negative peak is formed for sI|sII at $\lambda^+ = 353$ and $y^+ = 11.6$ which is in the vicinity of the peak in sII. The normalised peak value is $\varphi_{uu,\,\mathrm{sI|sII}} = -0.34$ which is very close in magnitude to that of the spectral peak of sII with $\varphi_{uu,\,\mathrm{sII}} = 0.37$. This shows that the energy which is added to the flow by sII is almost entirely compensated by the superposition of sI and sII. A similar behaviour is observed in all the spectral maps

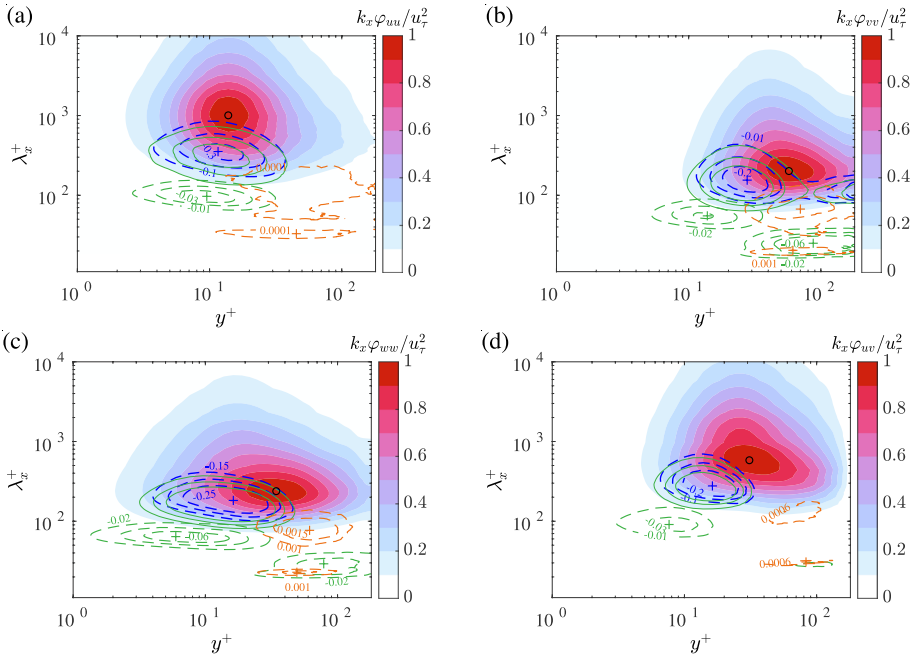

Fig. 13 Premultiplied velocity spectra φ_{uu} **a**, φ_{vv} **b**, φ_{ww} **c** and φ_{uv} **d**. Coloured contours correspond to the snapshots. Subspace interactions sI|sII, sII|sIII and sI|sIII are plotted in blue, green and orange dashed lines respectively. All the spectra have been normalised by the variance of the corresponding velocity component and by the peak value in the snapshots spectra

in Fig. 13. In order to illustrate the latter, contour lines of velocity spectra are plotted in solid green lines with contour levels identical to those of the sI|sII. It is clearly seen that the dashed blue lines and green solid lines coincide closely in all the plots. A very similar trend exists for the sII|sIII and sI|sIII. This explains how sI can have 97% contribution to turbulent kinetic energy.

The peaks closest to the wall in this figure are the ones formed by sII|sIII with the peaks magnitude being one order of magnitude smaller than those in sI|sII. The peaks in the spectral map of sI|sIII is also one order of magnitude smaller than those of sII|sIII with small but positive peak values, which adds a minimal level of energy to the overall kinetic energy. Another pattern observed in all sub-figures is the overall elliptical shape of the contour lines with their major axes being almost parallel to y^+ axis. This is opposed to the concentric circular contour lines which are mainly present in the *uu* spectral map for small y^+ values. The extended elliptical contours show a much larger slope when moving on a vertical line with constant $y+$. This means that the energy content per wave number changes slowly as y^+ increases and changes more rapidly as wave numbers change.

4.8 Anisotropy Invariant Map of the Subspaces

We study the structure of turbulent flow in each subspace by investigating the invariants of anisotropic Reynolds stress tensor

$$a_{ij} = \frac{\tau_{ij}}{\tau_{kk}} - \frac{\delta_{ij}}{3}. \tag{13}$$

A triangular domain is introduced by Banerjee et al. (2007) as a barycentric anisotropy map inside which all realisable Reynolds stress invariants are located. The vertices of the triangle represent three limiting states of one-component (1c), two-component (2c) and three-component isotropic turbulence, located respectively at $\mathrm{x}_{1c} = (1, 0)$, $\mathrm{x}_{2c} = (0, 0)$ and $\mathrm{x}_{3c} = (1/2, \sqrt{3}/2)$ as shown in Fig. 14. Moving away from the isotropic vertex on the blue edge corresponds to axi-symmetric contraction which ends up at the disc-like anisotropy at $2c$ vertex. Alternatively, moving on the black edge towards the $1c$ vertex corresponds to axi-symmetric expansion leading to needle-like anisotropy. The red edge connecting $1c$ and $2c$ vertices depicts the two-component limit. This map is defined using a linear combination of positive scalar metrics. These metrics are functions of eigenvalues of a_{ij} being sorted as $\lambda_1 \geq \lambda_2 \geq \lambda_3$ and are used to defined the coordinate system (x_B, y_B) given by

$$\begin{aligned} x_B &= C_{1c}x_{1c} + C_{2c}x_{2c} + C_{3c}x_{3c} = C_{1c} + C_{3c}\frac{1}{2} \\ y_B &= C_{1c}y_{1c} + C_{2c}y_{2c} + C_{3c}y_{3c} = C_{3c}\frac{\sqrt{3}}{2} \end{aligned} \tag{14}$$

where

$$C_{1c} = \lambda_1 - \lambda_2, \quad C_{2c} = 2(\lambda_2 - \lambda_3), \quad C_{3c} = 3\lambda_3 + 1. \tag{15}$$

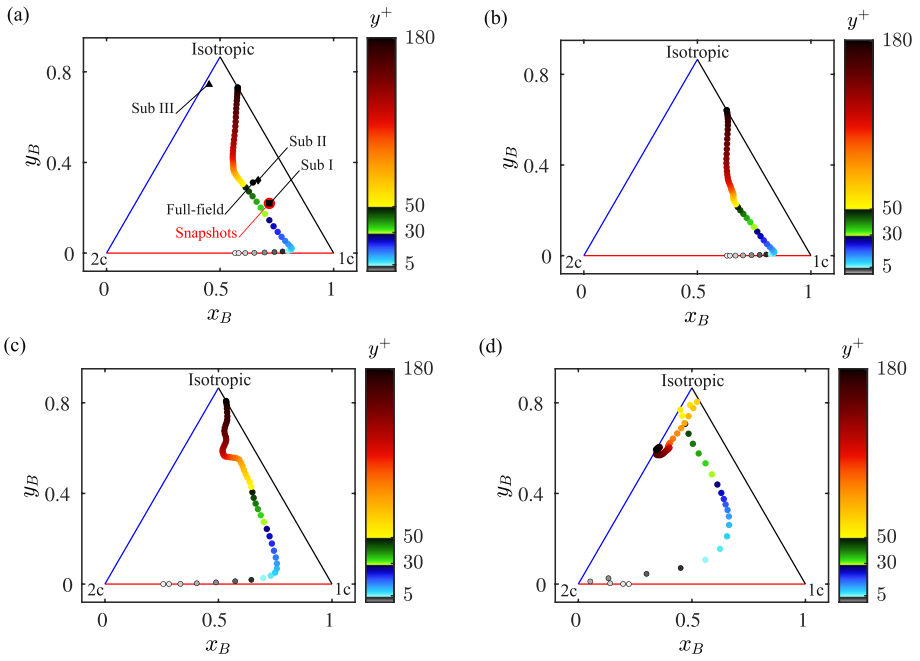

Fig. 14 Isotropy invariant map of the full field **a** subspace I **b**, subspace II **c** and subspace III **d**

To have a measure of the total anisotropy, a_{ij} is calculated using temporal averaging and weighted spatial averaging over all radial points and the results are plotted in annotated black markers in Fig. 14a. Subspaces I, II and III (shown with rectangle, diamond and triangle markers respectively) appear to be aligned on a line moving towards the isotropic state, with subspace III clearly being the most isotropic one. Snapshots averaged isotropy is plotted with a red circular marker being away from the full field due to the fewer number of timesteps available in the snapshots. Subspace I is almost exactly on top of the red marker showing a similar anisotropy to the snapshots.

The invariant map is plotted for the full field and for each wall-normal location in Fig. 14. To clearly inspect the isotropy state at each wall layer, a different colourmap has been chosen to distinguish four wall layers. Grey colourmap is set for the viscous sublayer, blue for the buffer layer between the viscous and logarithmic layer ($5 \leq y^+ \leq 30$), green for the logarithmic layer and a heat colourmap is chosen for the overlap and outer layer ($50 \leq y^+ \leq 181$). The map starts for the full field at the wall at the two-component limit in Fig. 14a and moves towards the one-component vertex. At $y^+ = 10$ in the buffer layer a sharp bend is observed after which the trajectory moves towards the centre of the map where a second bend is reached at $y^+ \approx 83$ followed by a straight path towards the isotropic vertex at the centre of the pipe.

The map for subspace I is plotted in Fig. 14b for each wall-normal location. The first bend takes place at the same location as the full field whereas the second bend appears earlier at $y^+ = 65$ followed by an S shaped movement towards the isotropic state. Similarly, subspace II starts on the wall on the two-component limit but closer to disc-like isotropy moving more rapidly towards the $1c$ vertex, reaching a softer bend at $y^+ = 10$. After that, the trajectory follows a straight line approaching the axi-symmetric expansion limit where the second bend takes place moving away from the black edge at $y^+ \approx 83$. A third bend is reached at $y^+ \approx 120$ after which the flow approaches the isotropic state close to the pipe axis.

Subspace III shows a very different behaviour starting on the two-component limit and moving towards the disc-like anisotropy where it almost reaches the $2c$ vertex in the viscous sublayer at $y^+ = 1.3$. A very soft bend takes place at $7.5 \leq y^+ \leq 14$ followed by a path towards the isotropic state. In the overlap layer at $57 \leq y^+ \leq 65$ the trajectory gets closest to the isotropic state after which it departs towards the axi-symmetric contraction limit at the pipe axis.

The anisotropy invariant map of subspace I resembles that of the snapshots very closely. This serves as another indication that subspace I successfully represents the main flow features with a minimal number of modes making it a reliable reduced order model of the flow to further investigate the embedded scales.

5 Summary and Conclusions

The wave-like definition of coherent structures in a characteristic frame of reference in transport-dominated turbulent flows proves to be very efficient for the two following reasons: The main features of pipe flow at $Re_b = 5300$ are captured accurately with only 3% of the modes which form an almost orthogonal subspace to the rest of the modes. This subspace reproduces 97% of the turbulent kinetic energy of the full flow, and more than 96% of the invariants of the Reynolds stress tensor. Its spectral signature matches the snapshots in terms of wall-normal locations and wavelengths of the premultiplied energy spectra.

This subspace serves as a low rank model of the flow representing the main flow properties discussed above. It accommodates the large-scale energetic streaks and low energy smaller scales responsible for the anisotropy map of the flow. Separating the streaks from the smaller scales in subspace I is the subject of a future study where interactions between different scales in sI will be investigated.

The second reason is that the remaining modes can be further divided into two subspaces based on their cumulative energy contributions to subspace I. The Third subspace accommodates very small scales with short turn-over times and persists as a turbulent background motion. The second subspace lives in between the mentioned subspaces I and III having faster decay rates than the other two subspaces with their spectral peak length scales being substantially smaller than the first and substantially larger than the third subspace.

We speculate that at higher Reynolds numbers more modes would be needed to build subspace I and the scale separation between the subspaces would increase. We base our speculation on the fact that the flow becomes more complex and wider range of group velocities would be present in the flow.

Acknowledgements All simulations in this study have been carried out on Norddeutscher Verbund für Hoch- und Höchstleistungsrechnen (HLRN) with project id: bbi00011, using the code of our project partners within the SPP 1881 (grant no. AV120/3-2).

Author contributions The first author developed the method and the code, performed the computations and formulated the manuscript. The third author conceived the idea of a decomposition in spatio-temporal space and supervised the analysis and interpretation of the results. All authors discussed the results and contributed to the final manuscript.

Funding Open Access funding enabled and organized by Projekt DEAL. This joint study was part of the Priority Programme SPP 1881 Turbulent Superstructures of the Deutsche Forschungsgemeinschaft and funded by grant no. SE 824/33-1 (J.S and A.Sh) and grant no. EG100/24-2 (Ch. E.).

Data availability Not applicable.

Declarations

Conflict of interest The authors report no Conflict of interest.

Ethics approval and consent to participate Not applicable.

Consent for publication Not applicable.

References

Álamo, J.C., Jiménez, J.: Linear energy amplification in turbulent channels. J. Fluid Mech. **559**, 205–213 (2006). https://doi.org/10.1017/S0022112006000607

Bailey, S.C.C., Smits, A.J.: Experimental investigation of the structure of large- and very-large-scale motions in turbulent pipe flow. J. Fluid Mech. **651**, 339–356 (2010). https://doi.org/10.1017/S0022112009993983

Banerjee, S., Krahl, R., Durst, F., Zenger, C.: Presentation of anisotropy properties of turbulence, invariants versus eigenvalue approaches. J. Turbul. **8**, 32 (2007). https://doi.org/10.1080/14685240701506896

Bauer, C., Kameke, A., Wagner, C.: Kinetic energy budget of the largest scales in turbulent pipe flow. Phys. Rev. Fluids **4**, 064607 (2019). https://doi.org/10.1103/PhysRevFluids.4.064607

Chernyshenko, S.I., Baig, M.F.: The mechanism of streak formation in near-wall turbulence. J. Fluid Mech. **544**, 99–131 (2005). https://doi.org/10.1017/S0022112005006506

Del Álamo, J.C., Jiménez, J.: Estimation of turbulent convection velocities and corrections to taylor's approximation. J. Fluid Mech. **640**, 5–26 (2009). https://doi.org/10.1017/S0022112009991029

El Khoury, G.K., Schlatter, P., Noorani, A., Fischer, P., Brethouwer, G., Johansson, A.: Direct numerical simulation of turbulent pipe flow at moderately high reynolds numbers. Flow Turbul. Combust. **91**, 475–495 (2013). https://doi.org/10.1007/s10494-013-9482-8

Feldmann, D., Bauer, C., Wagner, C.: Computational domain length and reynolds number effects on large-scale coherent motions in turbulent pipe flow. J. Turbul. **19**(3), 274–295 (2018). https://doi.org/10.1080/14685248.2017.1418086

Guala, M., Hommema, S.E., Adrian, R.J.: Large-scale and very-large-scale motions in turbulent pipe flow. J. Fluid Mech. **554**, 521–542 (2006). https://doi.org/10.1017/S0022112006008871

Hellström, L.H.O., Smits, A.J.: The energetic motions in turbulent pipe flow. Phys. Fluids **26**(12), 125102 (2014)

Hemati, M., Williams, M., Rowley, C.: Dynamic mode decomposition for large and streaming datasets. Phys. Fluids (2014). https://doi.org/10.1063/1.4901016

Hugues, S., Randriamampianina, A.: An improved projection scheme applied to pseudospectral methods for the incompressible navier-stokes equations. Int. J. Numer. Meth. Fluids **28**, 501–521 (1998)

Jiménez, J., Moin, P.: The minimal flow unit in near-wall turbulence. J. Fluid Mech. **225**, 213–240 (1991). https://doi.org/10.1017/S0022112091002033

Kim, K.C., Adrian, R.J.: Very large-scale motion in the outer layer. Phys. Fluids (1999). https://doi.org/10.1063/1.869889

Kline, S.J., Reynolds, W.C., Schraub, F.A., Runstadler, P.W.: The structure of turbulent boundary layers. J. Fluid Mech. **30**(4), 741–773 (1967). https://doi.org/10.1017/S0022112067001740

Lumley, J.L.: The structure of inhomogeneous turbulent flows. Atmospheric turbulence and radio wave propagation, 166–178 (1967)

López, J.M., Feldmann, D., Rampp, M., Vela-Martín, A., Shi, L., Avila, M.: nscouette - a high-performance code for direct numerical simulations of turbulent taylor-couette flow. SoftwareX **11**, 100395 (2020). https://doi.org/10.1016/j.softx.2019.100395

Marusic, I., McKeon, B., Monkewitz, P., Nagib, H., Smits, A., Sreenivasan, K.: Wall-bounded turbulent flows at high reynolds numbers: recent advances and key issues. Phys. Fluids (2010). https://doi.org/10.1063/1.3453711

Monty, J.P., Hutchins, N., Ng, H.C.H., Marusic, I., Cchon, M.S.: A comparison of turbulent pipe, channel and boundary layer flows. J. Fluid Mech. **632**, 431–442 (2009). https://doi.org/10.1017/S0022112009007423

Paeth, A.W.: Graphics gems, pp. 179–195. Academic Press Professional, Inc., San Diego, CA, USA (1990). Chap. A Fast Algorithm for General Raster Rotation

Pirozzoli, S., Romero, J., Fatica, M., Verzicco, R., Orlandi, P.: One-point statistics for turbulent pipe flow up to $re_\tau \approx 6000$. J. Fluid Mech. **926**, 28 (2021). https://doi.org/10.1017/jfm.2021.727

Reiss, J., Schulze, P., Sesterhenn, J., Mehrmann, V.: The shifted proper orthogonal decomposition: a mode decomposition for multiple transport phenomena. SIAM J. Sci. Comput. **40**(3), 1322–1344 (2018). https://doi.org/10.1137/17M1140571

Rosenberg, B.J., Hultmark, M., Vallikivi, S.C.C.B., Smits, A.J.: Turbulence spectra in smooth- and rough-wall pipe flow at extreme reynolds numbers. J. Fluid Mech. **731**, 46–63 (2013)

Rowley, C.W., Marsden, J.E.: Reconstruction equations and the karhunen-loève expansion for systems with symmetry. Physica D **142**(1–2), 1–19 (2000)

Schmid, P.J.: Dynamic mode decomposition of numerical and experimental data. J. Fluid Mech. **656**, 5–28 (2010)

Schmid, P.J., Sesterhenn, J.: Dynamic mode decomposition of numerical and experimental data. Amer. Phys. Soc.,61st APS meeting, 208 (2008)

Sesterhenn, J., Shahirpour, A.: A characteristic dynamic mode decomposition. Theor. Comput. Fluid Dyn. (2019). https://doi.org/10.1007/s00162-019-00494-y

Shi, L., Rampp, M., Hof, B., Avila, M.: A hybrid mpi-openmp parallel implementation for pseudospectral simulations with application to taylor-couette flow. Comput. Fluids **106**, 1–11 (2015). https://doi.org/10.1016/j.compfluid.2014.09.021

Sirovich, L.: Turbulence and the dynamics of coherent structures. i - coherent structures. ii - symmetries and transformations. iii - dynamics and scaling. Q. Appl. Math. **45**, 561–571 (1987)

Toh, S., Itano, T.: Interaction between a large-scale structure and near-wall structures in channel flow. J. Fluid Mech. **524**, 249–262 (2005). https://doi.org/10.1017/S002211200400237X

Vallikivi, M., Ganapathisubramani, B., Smits, A.J.: Spectral scaling in boundary layers and pipes at very high reynolds numbers. J. Fluid Mech. **771**, 303–326 (2015)

Yao, J., Rezaeiravesh, S., Schlatter, P., Hussain, F.: Direct numerical simulations of turbulent pipe flow up to $re_\tau \approx 5200$. J. Fluid Mech. **956**, 18 (2023). https://doi.org/10.1017/jfm.2022.1013

Yu, M., Ceci, A., Pirozzoli, S.: Reynolds number effects and outer similarity of pressure fluctuations in turbulent pipe flow. Int. J. Heat Fluid Flow **96**, 108998 (2022). https://doi.org/10.1016/j.ijheatfluidflow.2022.108998

Álamo, J.C., Jiménez, J.: Spectra of the very large anisotropic scales in turbulent channels. Phys. Fluids **15**(6), 41–44 (2003)